ELSEVIER

Chemical Engineering Journal 112 (2005) 197–210

Chemical Engineering Journal

www.elsevier.com/locate/cej

An investigation of the effect of viscosity on mixing in an oscillatory baffled column using digital particle image velocimetry and computational fluid dynamics simulation

Andrew W. Fitch, Hongbing Jian, Xiongwei Ni *

Centre for Oscillatory Baffled Reactor Applications (COBRA), Chemical Engineering, School of Engineering and Physical Sciences,
Heriot-Watt University, Edinburgh, EH 14 4AS, UK

Received 26 October 2004; received in revised form 30 June 2005; accepted 12 July 2005

Abstract

In this paper, we examine the effect of viscosity on the performance of the oscillatory baffled column (OBC) using the digital particle image velocimetry (DPIV) technique and computational fluid dynamics (CFD) codes. A selection of Newtonian (1–210 cP) and shear thinning fluids is investigated. The effects of viscosity on mixing are carefully observed by analysing flow patterns generated by both the DPIV and CFD methods. A ratio of the plane-averaged axial over the radial velocity is defined to quantify such the viscosity effects. For the given geometry the velocity ratio approaches to 2 very quickly at increased oscillatory Reynolds numbers, regardless of the Newtonian and non-Newtonian fluids used. An empirical critical ratio of 3.5 is identified, below which the system mixes sufficiently. This would act as the guide for industrial applications where a viscous fluid is mixed in an aqueous solution in the OBC.

Keywords: Oscillatory baffled column; Digital particle image velocimetry; Velocity vector maps; Viscosity; Newtonian fluids and non-Newtonian fluids; Computational fluid dynamics; Digital particle image velocimetry

1. Introduction

A vast number of chemical and biochemical engineering unit operations requires the mixing of fluids of viscous nature, such as in polymerisation, fermentation, organic synthesis and processing in speciality and pharmaceutical industries. These liquids often display shear thinning, time dependency or elasticity behaviours. It is well known that viscosity plays a significant role affecting flow, mixing and transport in reactor systems. A better understanding of the behaviour of viscous fluids on mixing is thus essential.

The first flow visualisations of viscous fluids in stirred tanks were reported in the 1950s [1,2] and such research have spanned several decades. For example, Metzner and Taylor [2] reported that the averaged shear rate in a stirred tank was proportional to the impeller speed; Greene et al. [18] presented flow visualisation of pseudo-plastic and visco-elastic fluids in the laminar and transitional flows. In the late 1980s to early 1990s, researchers were able to measure flow velocities before and after these transitions for both Newtonian and shear thinning fluids [3–8]. The primary technique used for flow visualisations in these investigations was the laser Doppler velocimetry (LDV). Nouri and Hockey [19] reviewed the research to date and also reported their experimental results for a glycerine and carboxymethylcellulose (CMC) salt solution at different power settings of a 60° pitched blade impeller, using LDV. The work reported in this paper is, however, concerned with quantifying flow characteristics of Newtonian and shear thinning solutions within an oscillatory baffled column (OBC), a different reactor configuration, under various operating conditions.

The OBC is a unique mixing device in that its radial velocity components are of a similar order of magnitude as axial ones. The mixing mechanism for this type of device can be understood with the help of Fig. 1. Fundamentally there must

---

* Corresponding author. Tel.: +44 131 451 3781; fax: +44 131 451 3129.
E-mail address: X.Ni@hw.ac.uk (X. Ni).

1385-8947/$ – see front matter © 2005 Elsevier B.V. All rights reserved.
doi:10.1016/j.cej.2005.07.013

Nomenclature

D	diameter of column (mm)
f	oscillation frequency (Hz)
K	consistency index
$\dot{m}$	mass flow rate ($\mathrm{kg\,s^{-1}}$)
n	power-law index
Re_o	oscillatory Reynolds number
R_v	velocity ratio
St	Strouhal number
t	time (s)
T	temperature (K)
x_o	oscillating amplitude (mm) (centre to peak)
x	radial co-ordinates (mm)
y	axial co-ordinates (mm)

Greek letters

$\bar{\dot{\gamma}}$	strain rate tensor ($\mathrm{s^{-1}}$)
η	apparent viscosity ($\mathrm{kg\,m^{-1}\,s^{-1}}$)
μ	fluid viscosity ($\mathrm{kg\,m^{-1}\,s^{-1}}$)
ρ	fluid density ($\mathrm{kg\,m^{-3}}$)
τ	shear stress ($\mathrm{kg\,m^{-1}\,s^{-2}}$)

be sharp edges (provided by the baffles) presented transverse a fully reversing flow. The periodic motion of the fully reversing flow accelerates and decelerates according to a sinusoidal velocity–time function. The flow acceleration produces a vortex ring down stream of the baffle encompassing the width of the column. As the flow decelerates these vortices are swept into the centre of the column producing a well-mixed region. This mechanism offers a uniform and enhanced mixing within each baffled cavity as well as along the length of the column.

There are two dimensionless groups that govern the fluid mechanical conditions in a batch OBC: the oscillatory Reynolds number (Re_o) and the Strouhal number (St), which are defined as:

$$Re_\mathrm{o} = \frac{2\pi f x_\mathrm{o} \rho D}{\mu} \tag{1}$$

$$St = \frac{D}{4\pi x_\mathrm{o}} \tag{2}$$

where ρ is the fluid density ($\mathrm{kg\,m^{-3}}$), D the diameter of the column (m), x_o the oscillation amplitude (m, centre to peak), f the oscillation frequency (Hz) and μ is the fluid viscosity ($\mathrm{kg\,m^{-1}\,s^{-1}}$). The oscillatory Reynolds number describes the intensity of mixing applied to the column, while the Strouhal number is the ratio of column diameter to stroke length, characterising the effective eddy propagation [9–11].

In this study, the well-established digital particle image velocimetry (DPIV) [12–14] is used in combination with a computational fluid dynamics (CFD) technique. Our previous studies show that we are able to model the 3D flow patterns within an OBC [15] using the CFD codes and able to validate the modelled results using the DPIV measurements [15–17].

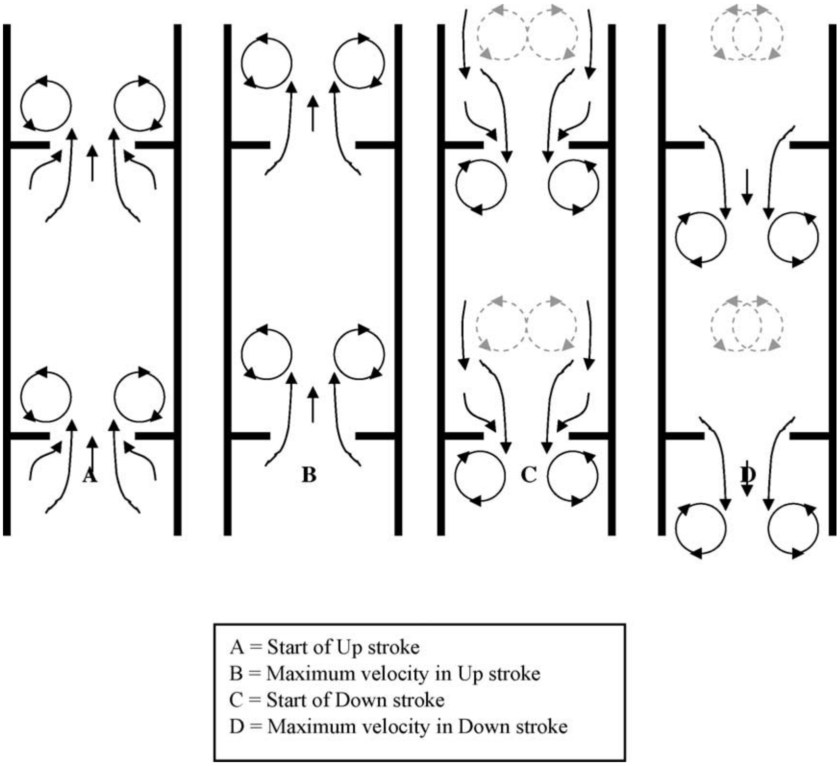

Fig. 1. Mechanism of mixing in an oscillatory baffled column.

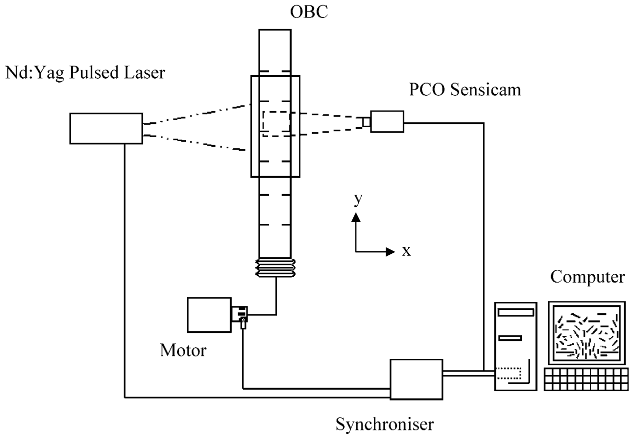

Fig. 2. A schematic diagram of the OBC and DPIV set up.

However, characterisations of flow in the OBC using both the DPIV and CFD methodologies have so far been limited to water as the measuring medium, in this investigation, we report, for the first time, our studies into the effect of viscosity on the performance of the OBC.

2. Experimental facilities and DPIV set up

2.1. Oscillatory baffled column

The OBC in Fig. 2 is made of a Perspex column, 50 mm in internal diameter and 500 mm in height. It has a volume capacity of 1 dm^3 and operates in a batch mode. For optical analysis a rectangular view box is sealed around the column at the point of investigation to remove geometrical distortions introduced by the circular nature of the column. The oscillation is driven by a stainless steel bellows, at the base of the column, attached to motor via a crank arm. The motor speed controls the oscillation frequency and the crank arm offset controls the oscillation amplitude. This combination provides frequencies from 0.5 to 10 Hz and amplitudes from 2 to 6 mm. Attached to the motor arm is a disc with eight equally sized and spaced slots, which rotates with the motor. Clamped to the framework of the system is an optical detector through which the disc spins. This generates eight pulses per cycle of oscillation as shown in Fig. 3 and these pulses will trigger the DPIV system. The breaking down of the oscillation cycle into phases also allows convenience in handling simulation data and easy in comparing data between the DPIV and CFD methods.

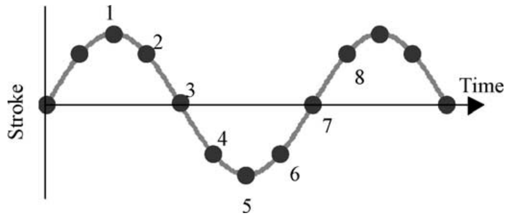

Fig. 3. Phase position with respect to time.

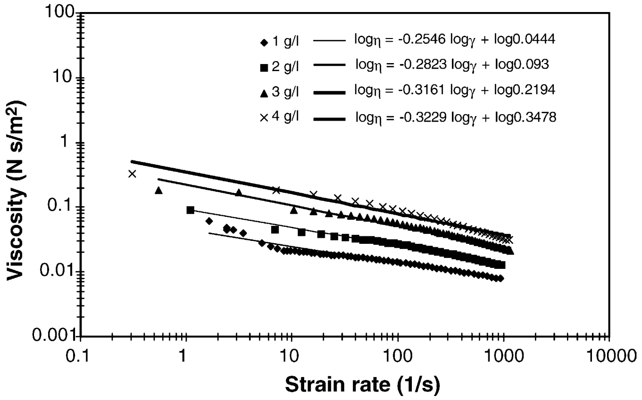

Fig. 4. Viscous properties of the CMC–water fluids investigated (symbols—experimental measurements; lines of different intensity—fits from numerical simulations).

2.2. DPIV system

The two-dimensional DPIV system is schematically shown in Fig. 2. It consists of a Nd:Yag double pulsed laser by New Wave Research (USA) with appropriate lenses to create a light sheet, which is aligned so that the vertical light sheet is located along the centreline of the OBC. A PCO SensiCam cross-correlation camera (Germany), a 1300 × 1000 pixel resolution, is used to acquire double images at a maximum rate of 4 Hz. The timing of the laser and the camera is controlled by a synchroniser, supplied by Optical Flow Systems (Scotland). The synchroniser accepts the external trigger, created from the disc on the motor arm depicting the phase of oscillation (Fig. 3), sends a pulse to the laser and camera. The camera then feeds back the image pair to the computer for analysis. VidPIV 4, the software from Optical Flow Systems, is capable of controlling the timing of the synchroniser by programming it between light sheets, as well as

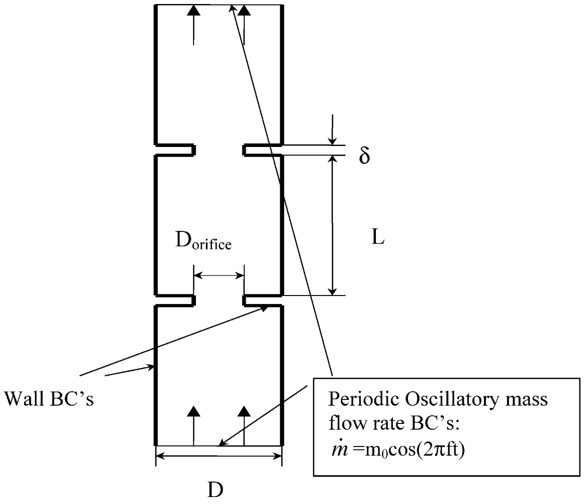

Fig. 5. Basic configuration of OBC and periodic boundary conditions.

of performing the cross-correlation analysis to create vector maps.

2.3. Experimental procedure

The OBC is filled with 1 dm^3 of fluid, seeded with neutrally buoyant hollow glass silvered spheres of 10 μm in diameter and oscillated at a pre-set frequency and amplitude. Fifteen image pairs are recorded for each of the eight phases in an oscillation cycle. These have been carried out for three oscillation amplitudes (2, 4 and 6 mm centre to peak) and three oscillation frequencies (1, 2 and 3 Hz), corresponding to $Re_o = 628–5655$ (for water). The image pairs are then analysed using the cross-correlation method in VidPIV 4. Velocity vector maps, strain rate derivations and plane-averaged properties are calculated and presented. The process is then repeated for each fluid being investigated. Two types of fluids are used in our study: glycerol–water solutions and CMC–water solutions. The former represents the Newtonian fluid and the latter the non-Newtonian fluid. Glycerol concentrations vary from 0, 10, 50, 70 and 90% of the total volume, corresponding to a viscosity of 1, 2.5, 8, 70 and 210 cP, respectively. Four CMC concentrations of 1, 2, 3 and 4 g/dm^3 of water were used in the study; the non-Newtonian

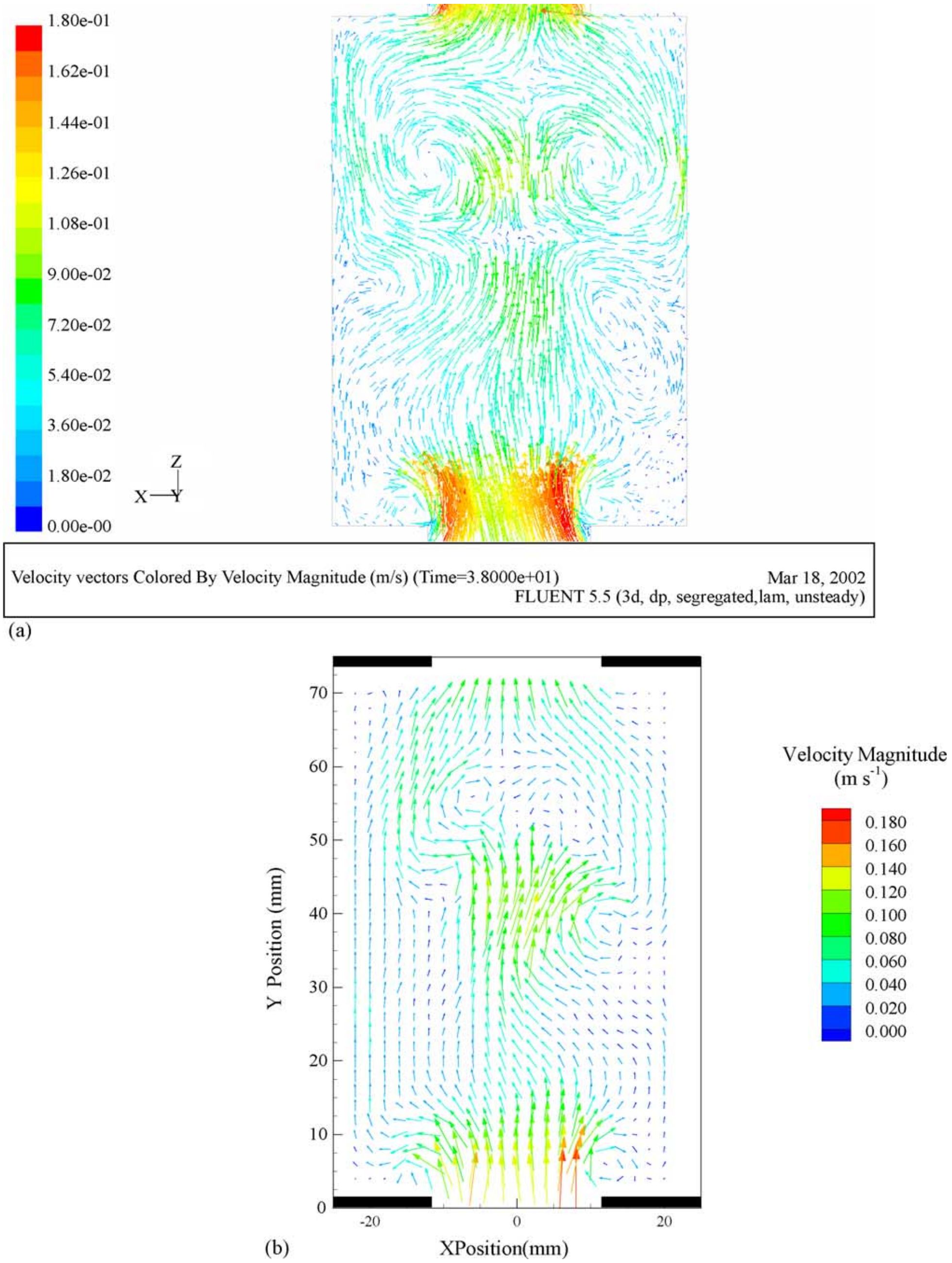

Fig. 6. Water vector flow map: (a) CFD, (b) DPIV; phase 7 $Re_o = 1257$, $St = 1.0$, $x_o = 4$ mm, $f = 1$ Hz, $\mu = 1$ cP.

behaviours of the CMC fluids are shown in a log–log plot of Fig. 4. More discussions on Fig. 4 will be given later.

3. Numerical set up

The CFD code used in this study is the 3D unsteady laminar solver based on a Fluent 5 package, which was previously described [15]. The numerical simulations work on the same geometry as the experiments utilising two-orifice baffles of the OBC, i.e. three baffled cells, as shown in Fig. 5. The column diameter is 50 mm, the baffle spacing 75 mm and the orifice diameter 23 mm. Density and temperature variations are ignored in the simulation. For the Newtonian fluids such as glycerol solutions, the shear stress (τ) is linearly proportional to the strain rate tensor ($\bar{\dot{\gamma}}$):

$$\tau = \mu\bar{\dot{\gamma}} \tag{3}$$

where $\bar{\dot{\gamma}} = \left(\frac{\partial u_i}{\partial x_j} + \frac{\partial u_j}{\partial x_i}\right)$, where u_i ($i = x, y, z$) and u_j ($j = y, z, x$) are the Cartesian instantaneous velocities (m s^{-1}) and μ is the viscosity, which is constant and independent of the strain rate. However, for the non-Newtonian CMC fluids, the apparent viscosity will be modelled according to the following power

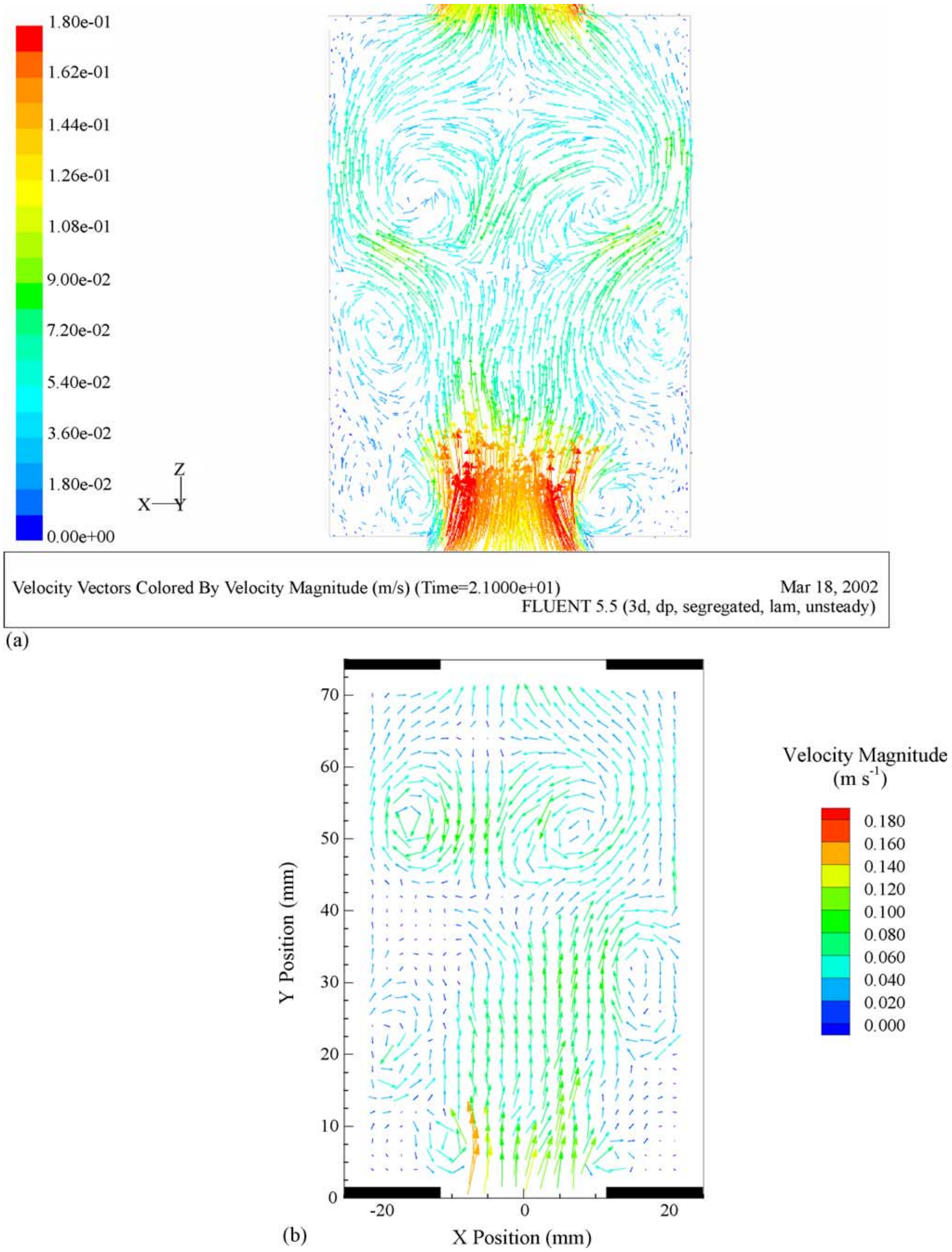

Fig. 7. DPIV Newtonian vector flow map: (a) CFD, (b) DPIV; phase 7 $Re_o = 503$, $St = 1.0$, $x_o = 4$ mm, $f = 1$ Hz, $\mu = 2.5$ cP.

law equation:

$$\eta = K(\bar{\dot{\gamma}})^{n-1}(\mathrm{kg\,m^{-1}\,S^{-1}}) \tag{4}$$

where K is a measure of the average viscosity of the fluid (the consistency index), and n is the power-law index, which is a measure of the fluids deviation from the Newtonian behaviour. It should be noted that the strain rate tensor, $\bar{\dot{\gamma}}$, in Eqs. (3) and (4) requires a total of nine components, which are directly generated by the CFD codes, however, the current 2D DPIV can only provide four of them. What are missing from the direct DPIV measurements are the derivatives of the circumferential velocity and derivatives with respect to the circumferential axis, i.e. $\frac{\partial u_z}{\partial x}$, $\frac{\partial u_z}{\partial y}$, $\frac{\partial u_z}{\partial z}$, $\frac{\partial u_x}{\partial z}$, $\frac{\partial u_y}{\partial z}$. Due to large-scale anisotropic motion in the flow, the missing strain rate components cannot be approximated from the known terms theoretically. However, examination of the four known components of their dissipation rate tensor using the Smagorisky model reveals that they all have similar distributions and magnitudes [17]. We can thus assume that the three-dimensional strain rate can be approximated by multiplying the sum of the known components by a factor of $\frac{9}{4}$, i.e. $\bar{\dot{\gamma}}_{3\mathrm{D}} \approx \frac{9}{4}\bar{\dot{\gamma}}_{2\mathrm{D}}$. Obvi-

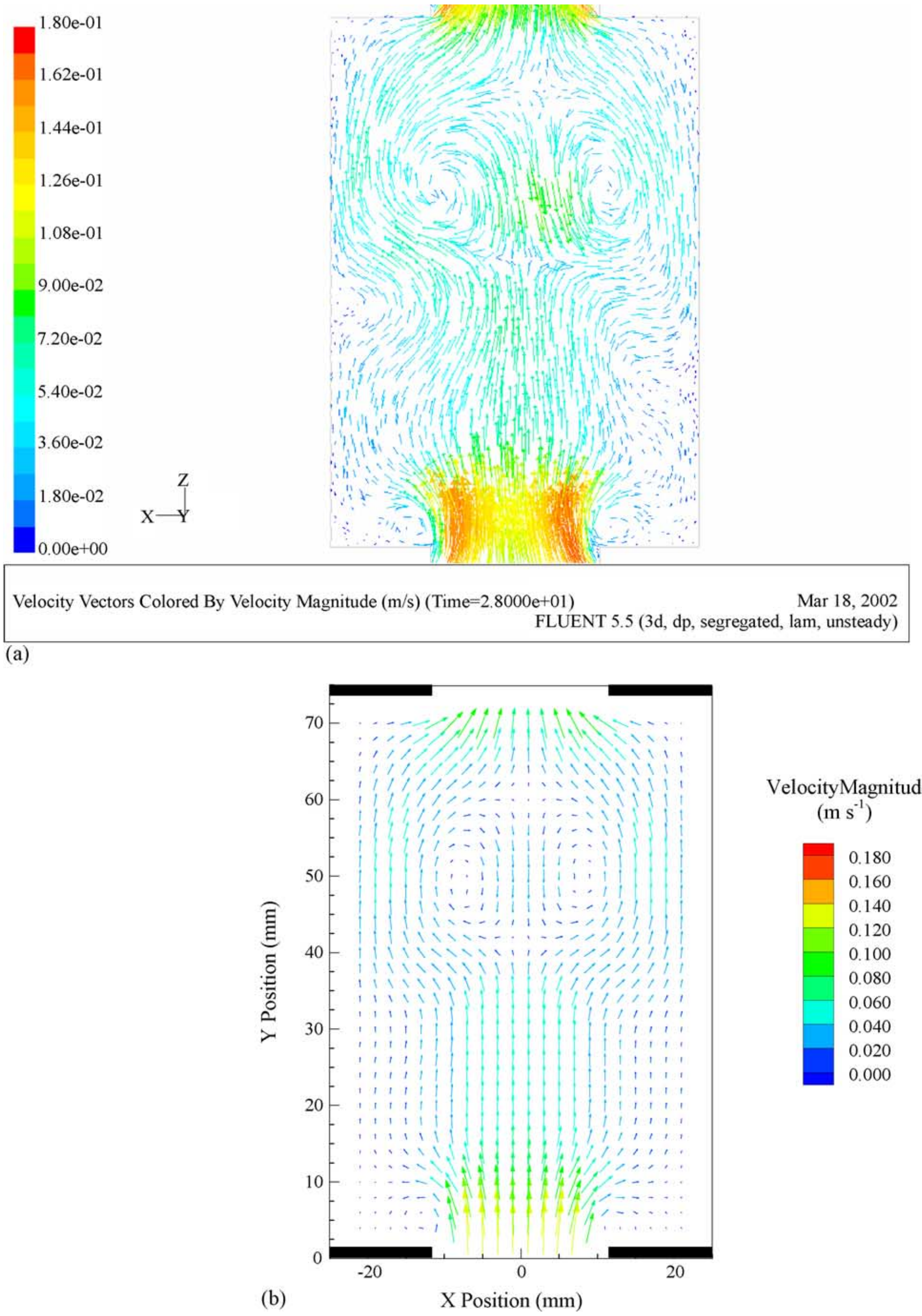

Fig. 8. DPIV Newtonian vector flow map: (a) CFD, (b) DPIV; phase 7 $Re_o = 157$, $St = 1.0$, $x_o = 4$ mm, $f = 1$ Hz, $\mu = 8$ cP.

ously further improvement of the strain rate approximation will require extension of the velocity measurement to 3D, but this simple method has proved to work to satisfaction [17].

For the purpose of CFD simulation using Fluent, the upper and lower limits on the power law function must be set, i.e. $\eta_{\min} < \eta = ke^{\frac{T_0}{T}}(\bar{\dot{\gamma}})^{n-1} < \eta_{\max}$, where T is the temperature of solution being meausred (K), T_0 the reference temperature (K). In our study, $T = T_0$, hence $ke^{\frac{T_0}{T}} = K$. Thus the input parameters for Fluent codes are K, n, $\eta_{\min}$ and $\eta_{\max}$. If the viscosity computed from the power law equation is less than $\eta_{\min}$, the value of $\eta_{\min}$ will then be used in the modelling, likewise for $\eta_{\max}$. The purpose of using a maximum and minimum apparent viscosity in Fluent is to avoid numerical problems with the infinite zero strain rate viscosity predicted by the power law model. It is worth noting that the iteration procedure in the Fluent codes allows the selection of the maximum and minimum apparent viscosity realistic to the data that are being modelled, see the values shown in Table 1.

In Fig. 4, the symbols are the experimental measurements, while the lines of different intensity are the modelled behaviour of the CMC solutions from the numerical simulations with the input parameters for each CMC solution

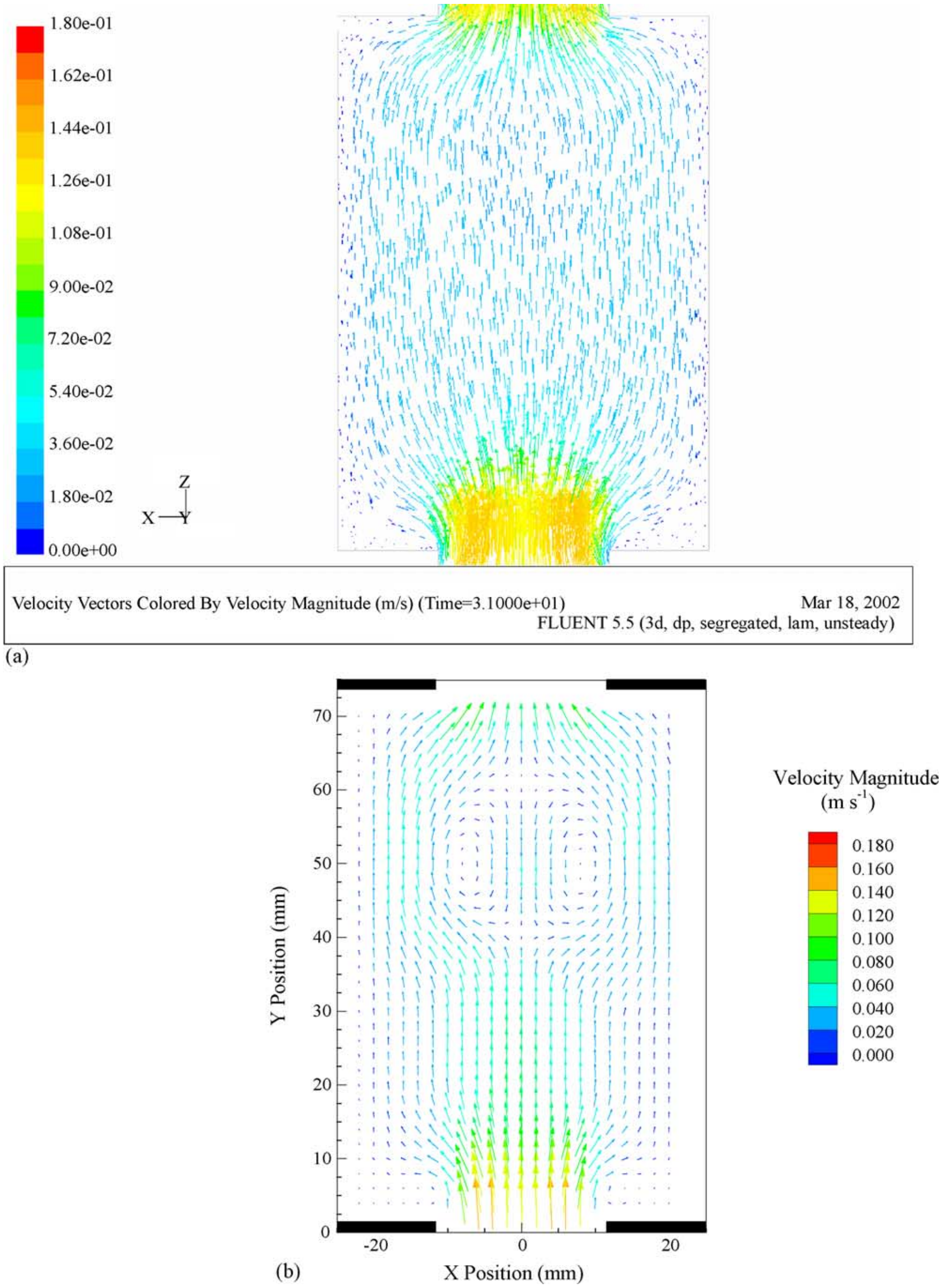

Fig. 9. DPIV Newtonian vector flow map: (a) CFD, (b) DPIV; phase 7 $Re_o = 18$, $St = 1.0$, $x_o = 4$ mm, $f = 1$ Hz, $\mu = 70$ cP.

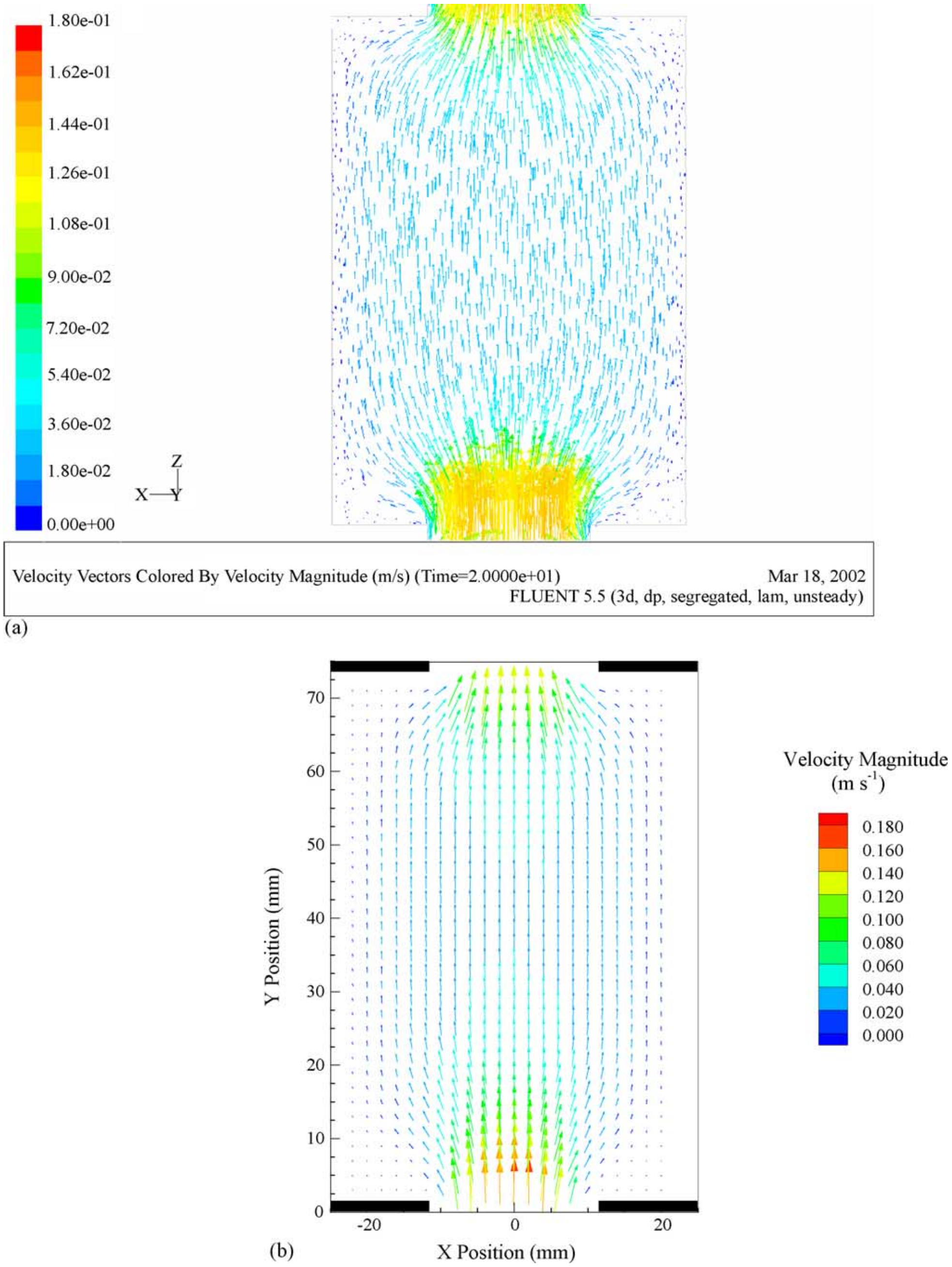

Fig. 10. DPIV Newtonian vector flow map: (a) CFD, (b) DPIV; phase 7 $Re_o = 6$, $St = 1.0$, $x_o = 4$ mm, $f = 1$ Hz, $\mu = 210$ cP.

summarised in Table 1. It can be observed from Fig. 4 that the viscosity generally decreases with the increase of the shear strain rate – the characteristic of a shear-thinning fluid – with some deviations in viscosity from the power law predictions for the lower end of the strain rate. Such deviations are mainly associated with the numerical process of fine-tuning the maximum and minimum apparent viscosity. Overall the fittings from the numerical simulation are pretty good. Depending on the strain rate, the apparent viscosity ranges from a few cP for the lowest CMC concentration to hundreds cP for the highest CMC solution.

Table 1
Input parameters of the power-law for the CMC fluids

CMC (g/l)	η_{max} (kg m^{-1} s^{-1})	η_{min} (kg m^{-1} s^{-1})	n	K
1	0.063	0.0075	0.7454	0.0444
2	0.096	0.013	0.7177	0.093
3	0.186	0.021	0.6839	0.2194
4	0.324	0.032	0.6771	0.3478

3.1. Boundary conditions

Boundary conditions should account for both the spatial periodicity and temporal periodicity in an OBC configuration. Non-slip conditions are used for the wall boundaries. For the spatial periodicity, the flow, as well as the grids at the inlet and outlet (see as the top and bottom surfaces shown in Fig. 5) is forced to be identical for each time step.

The temporal periodicity is implemented by discretising the mass flow rate of $\dot{m} = \rho\left(\frac{\pi}{4}D^2\right) 2\pi f x_{\mathrm{o}} \cos(2\pi f t)$ into many tiny known time intervals over an oscillation cycle. At each time interval, the mass flow rates at both inlet and outlet are calculated corresponding to the time as well as the phase positions of the oscillation and are then forced to be the same.

4. Comparison of flow visualisation

In our previous work [15], we have already demonstrated that we can use the 3D unsteady laminar solver to accurately predict and apply the DPIV technique to faithfully validate the flow patterns of a single liquid (water) in the OBC at various operating conditions. We now extend our studies to viscous fluids in the OBC. The CFD and DPIV results will be presented side by side to describe the behaviour of the viscous fluids in the OBC.

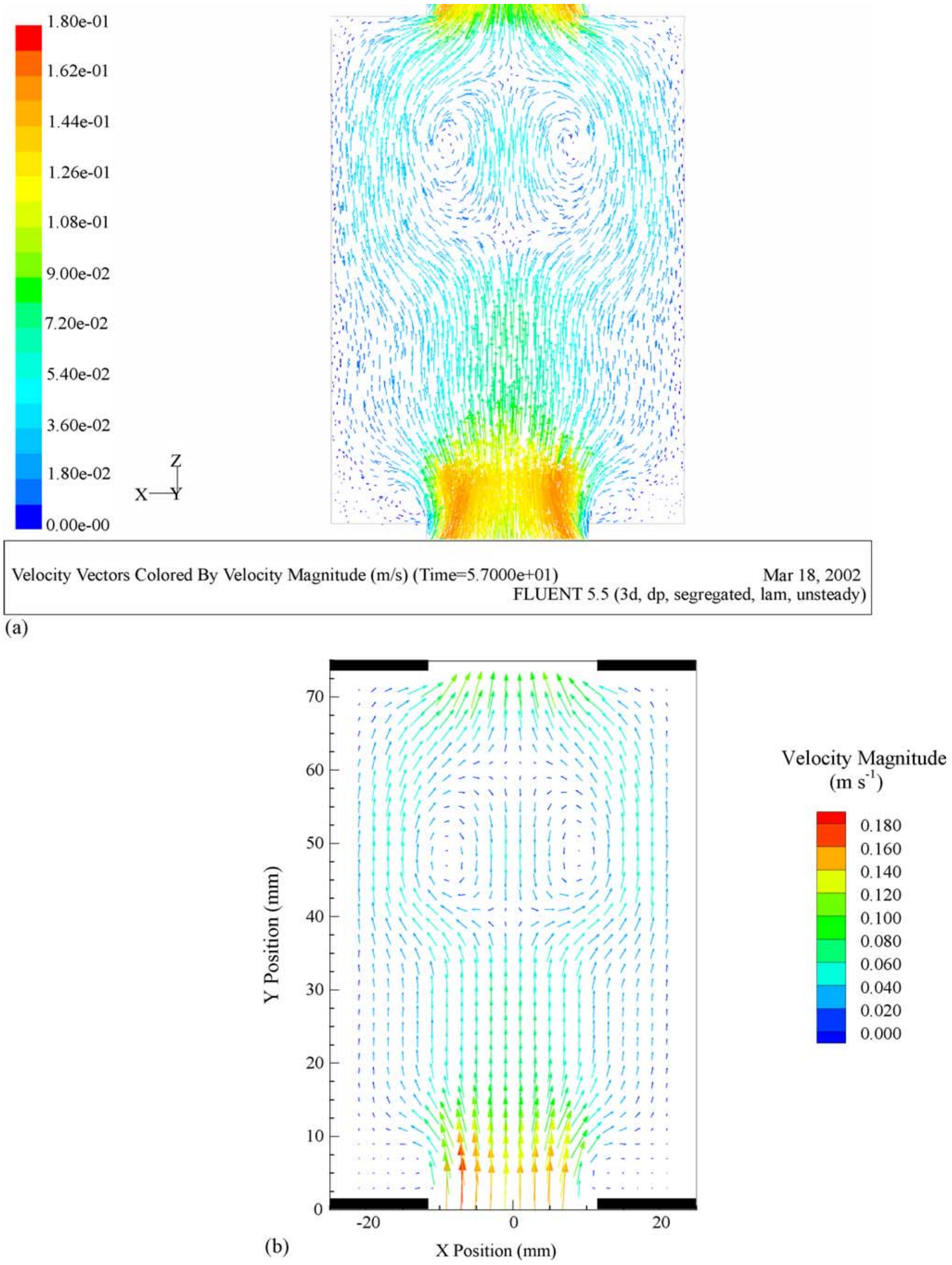

Fig. 11. DPIV non-Newtonian vector flow map: (a) CFD, (b) DPIV; phase 7 $Re_{\mathrm{o}} = 84$, $St = 1.0$, $x_{\mathrm{o}} = 4$ mm, $f = 1$ Hz, $\mu = 15$ cP.

4.1. Observations of flow patterns of Newtonian fluids

We investigated the behaviours of five different Newtonian fluids at a fixed operating condition, i.e. $x_o = 4$ mm, $f = 1$ Hz and $Re_o = 1250$. For the DPIV measurements, 15 image pairs are recorded for each of the eight phases in one oscillation cycle and a total of 15 cycles are used. Consequently, there are a large number of graphs generated from every phase of each oscillation cycle by the two methods, and for the purpose of presentation, only one phase from one cycle is selected. Fig. 6 shows the vector map for water ($\mu = 1$ cP) at the phase 7 of the oscillation cycle 5 for both CFD and DPIV methods. Figs. 7–10 shows the progression in the change in flow patterns of the Newtonian fluid with an increase in viscosity from 2.5 to 210 cP at the same operating conditions. The colour contours on the vector map represent the absolute velocity magnitude (m s^{-1}) where red is high and blue is low. As we examine the flow patterns from water (Fig. 6) to the low viscosity fluid (2.5 cP) (Fig. 7) we see strong vortex activities and interactions within the baffled cell, and there are little changes in vector movement and vortex formation between the two cases. The systems are well

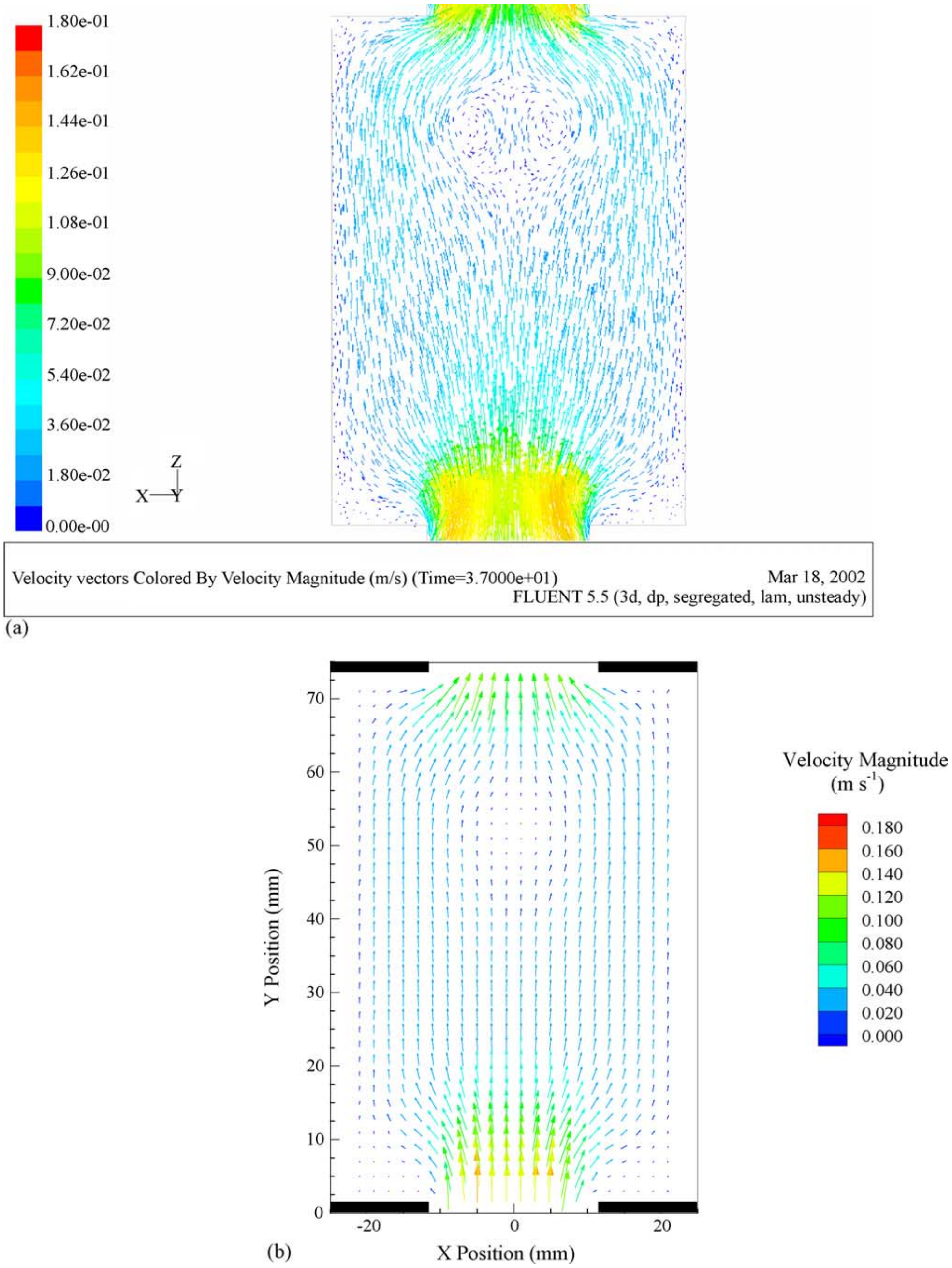

Fig. 12. DPIV non-Newtonian vector flow map: (a) CFD, (b) DPIV; phase 7 $Re_o = 50$, $St = 1.0$, $x_o = 4$ mm, $f = 1$ Hz, $\mu = 25$ cP.

mixed. For the solution of 8 cP (Fig. 8), there is again not much change in vortex positions compared with that shown in Figs. 6 and 7. The eddy motions are apparent and strong. As the viscosity increases to 70 cP (Fig. 9), the symmetrical flow patterns have developed; the vortex activities are notably decreased in the baffled cell. In Fig. 9 there is a discrepancy between the DPIV and CFD results, where the DPIV system still reports two diminishing and symmetrical eddies, while at this condition CFD simulation predicts a symmetrical flow pattern with no presence of eddies. The reason for this is not entirely understandable. However, what is clear is that these flow patterns evidently differ from that shown in Fig. 6. As the viscosity of the system increases further ($\mu = 210$ cP) we see a 'channelling' effect created through the centre of the unbaffled region with no vortices being formed at all (Fig. 10). This reveals that as the Newtonian viscosity increases the flow become increasingly symmetrical, and the axial flow becomes dominant, as a result, areas by the walls become less/not at all well mixed. The complete cycle observations and analysis of the flow patterns reveal that the flow becomes globally centralised to the area through the baffle's orifice as the viscosity increases significantly, and consequently the mixing in the system becomes poorer.

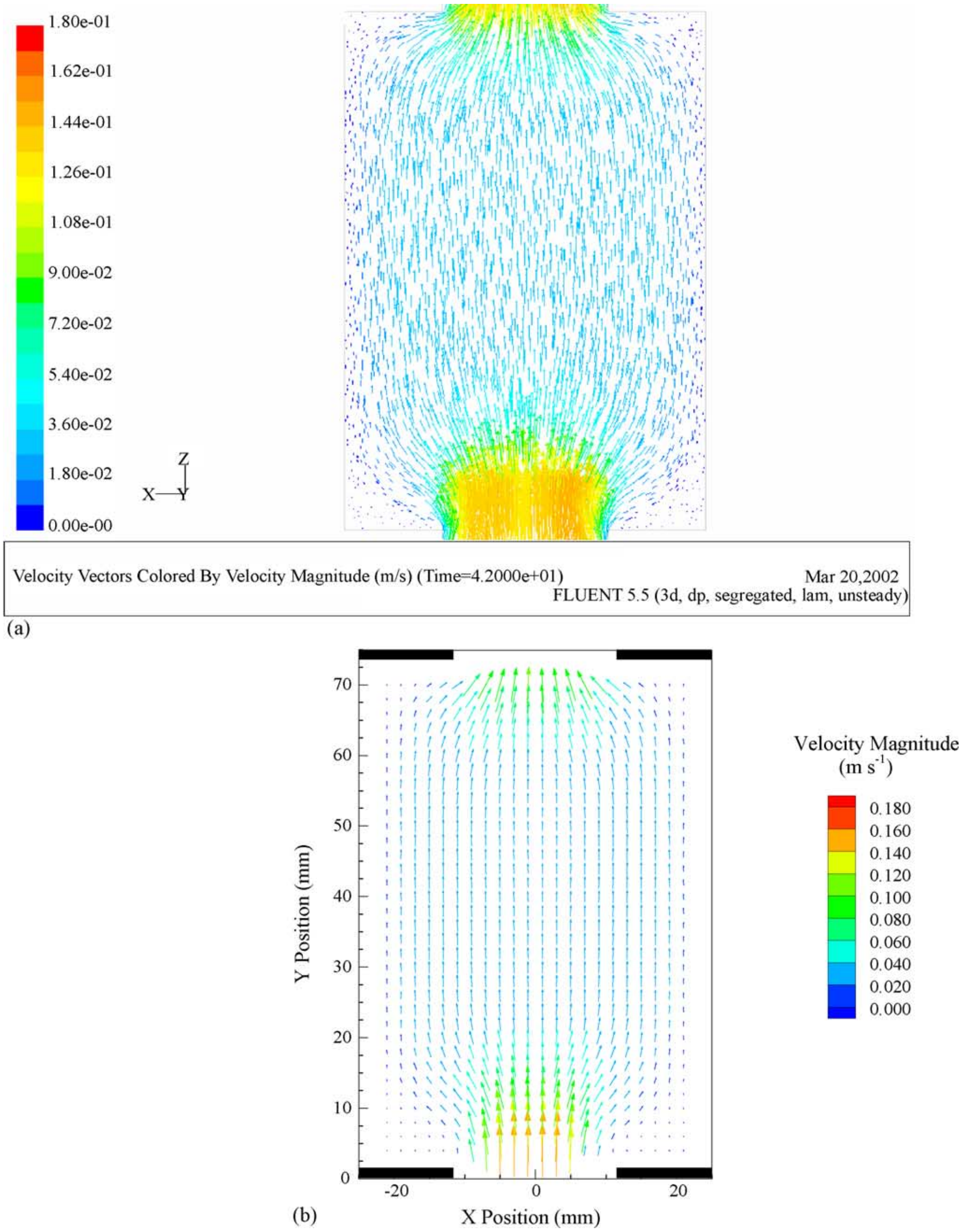

Fig. 13. DPIV non-Newtonian vector flow map: (a) CFD, (b) DPIV; phase 7 $Re_o = 23$, $St = 1.0$, $x_o = 4$ mm, $f = 1$ Hz, $\mu = 55$ cP.

4.2. Observations of flow patterns of shear thinning fluids

For the non-Newtonian fluids, the traditional approach is to avoid the terminology of the Reynolds number, since it is dependent upon the viscosity, which is a function of strain rate. In this study, the averaged or the equivalent oscillatory Reynolds number is employed. Firstly the spatially and temporally averaged shear strains are calculated, and the procedure can be summarised as: the strain rate ($\bar{\dot{\gamma}}_{2D}$) from the direct DPIV measurements is converted into 3D strain rate, i.e. $\bar{\dot{\gamma}}_{3D}(\approx \frac{9}{4}\bar{\dot{\gamma}}_{2D})$ The spatial averaged strain rate is computed via $\frac{\sum_{i}^{44}\sum_{j}^{69}\bar{\dot{\gamma}}_{3D}}{i_{\max} j_{\max}}$ over a planar area and then used to generate the temporal averaged strain rate via $\frac{\sum_{\text{cycle}}^{15}\sum_{\text{phase}}^{8}\bar{\dot{\gamma}}_{\text{spatial-averaged}}}{\text{cycle}_{\max}\times\text{phase}_{\max}}$ over the oscillation phases and cycles. The temporal averaged strain rate is therefore used to obtain an averaged viscosity, which is compared with that shown in Fig. 4, and in turn used to calculate the averaged or the equivalent oscillatory Reynolds number. Figs. 11–14 show the flow patterns for the four CMC fluids being investigated at the same operat-

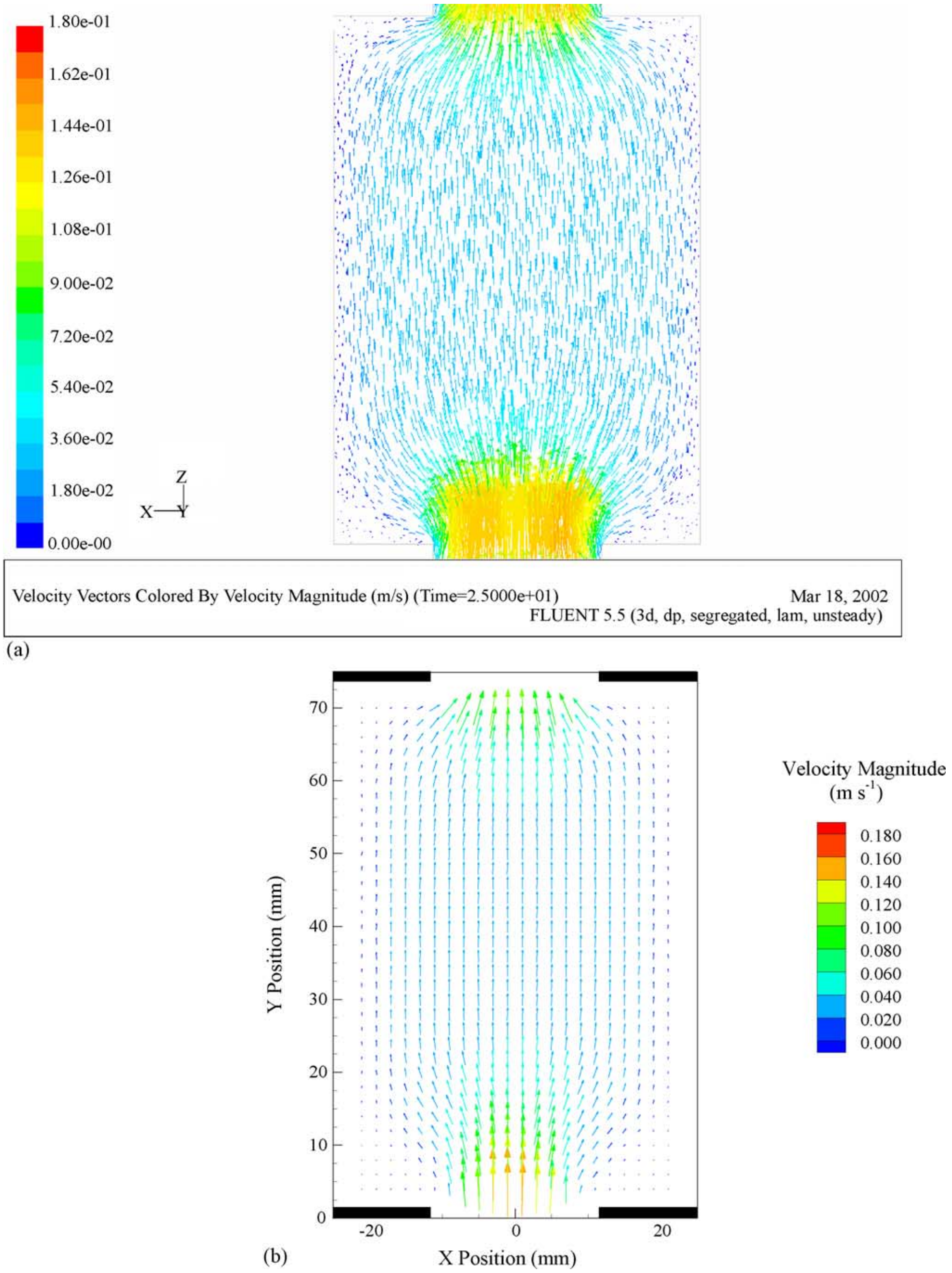

Fig. 14. DPIV non-Newtonian vector flow map: (a) CFD, (b) DPIV; phase 7 $Re_o = 13$, $St = 1.0$, $x_o = 4$ mm, $f = 1$ Hz, $\mu = 100$ cP.

ing conditions ($x_o = 4$ mm, $f = 1$ Hz) and at the same phase of oscillation as presented in the Newtonian case. All the oscillatory Reynolds numbers given in Figs. 11–14 are calculated according the above method.Evidently from the vector map of the 1 g/l CMC solution in Fig. 11 ($\mu = 15$ cP) there are active eddy motions, with some degrees of symmetry. As the CMC concentration increases to 2 g/l ($\mu = 25$ cP) in Fig. 12, both the eddy motion and the activity of interaction are weakened, and flow patterns are clearly symmetric. There are two small diminishing vortices shown in the CFD simulation, while the tail end of these eddies in the DPIV measurements. With the further increase in the CMC concentrations, the axial velocity components become dominant over the radial ones, and the channelling flow is the main characteristic in Figs. 13 and 14. Consequently the global mixing is poor.

5. Velocity ratio

Our CFD simulations and DPIV measurements of flow patterns for both Newtonian and non-Newtonian fluids have shown that the viscosity strongly affects the flow patterns, in turn the performance of mixing in the device. To look at this in detail we define, R_v, as the dimensionless ratio between the plane-averaged axial and radial velocities:

$$R_v = \frac{\sum_{j=1}^{J}\sum_{i=1}^{I}|u_{y(i,j)}|/J \cdot I}{\sum_{j=1}^{J}\sum_{i=1}^{I}|u_{x(i,j)}|/J \cdot I} \qquad (5)$$

where u_y and u_x are the velocity components in the y (axial) and x (radial) directions respectively. The plane average is the sum of velocity measurements in the measuring plane in both i and j directions divided by the product of the numbers in the two directions. This index describes the effective transport of the axial oscillatory velocity to the radial component, where the lower the value, the more effective the system.

Fig. 15 plots the velocity ratio of R_v against the oscillatory Reynolds number (Re_o) for both the Newtonian and the non-Newtonian fluids, for the latter it is the equivalent oscillatory Reynolds number. It is worth noting that a much wider range of operating conditions is used in the DPIV measurements than in the CFD simulations, in fact the former covers the full combinations of three oscillation amplitudes of 2, 4 and 6 mm and three oscillation frequencies of 1, 2 and 3 Hz with the oscillatory Reynolds numbers ranging from 628 to 5655; while the maximum oscillatory Reynolds number in the CFD simulations is 1250. At those increased operating conditions it will take significant longer CPU times for the CFD simulations, on balance we felt it was not necessary to do so, and the DPIV measurements would be sufficient. From Fig. 15, we see clearly that as the Re_o increases (viscosity decreases) the value of the velocity ratio decreases and approaches to 2 very quickly. The value of 2 indicates that the radial velocity is half of the axial velocity for well-mixed systems at the given geometrical parameters. Interestingly the trend for the non-Newtonian fluids is identical to that for the Newtonian fluids, as almost all the points between the two fluids are overlapped for the range of operational conditions used in this study. To look at this phenomenon more closely, we zoom in on the data points for the oscillatory Reynolds numbers between 0 and 1400, where both CFD and DPIV data are available. It can be seen that the agreement between the CFD and DPIV is quite good for both the Newtonian and non-Newtonian fluids. The velocity ratio of R_v changes between 3.8 and 2 for the oscillatory Reynolds numbers between 100 and 600. Based on the analysis and our experience, we define that when $R_v > 3.5$ the mixing would be ineffective, i.e. the effect of viscosity on mixing would be significant.

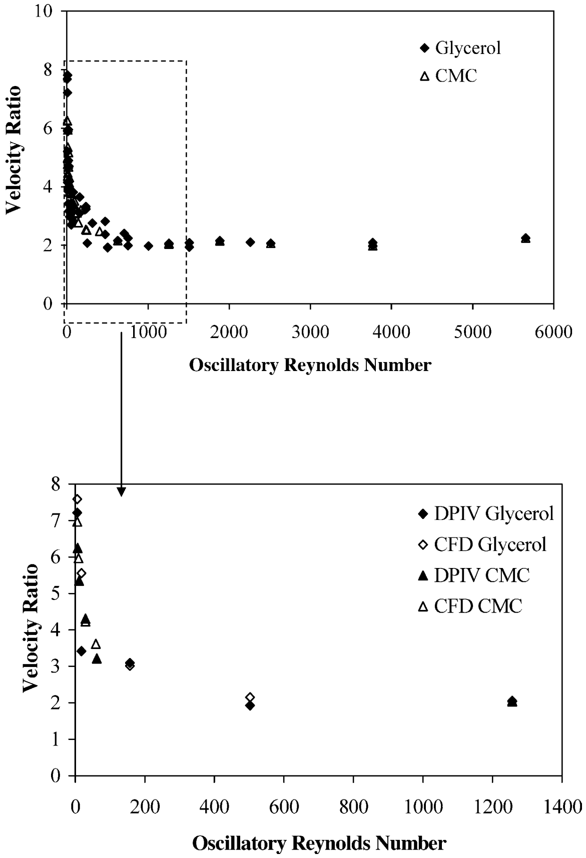

Fig. 15. Velocity ratio vs. oscillatory Reynolds number for both Newtonian and non-Newtonian fluids.

In the process of mixing it is essential that there is sufficient agitation to encompass the whole vessel. When viscous fluids are introduced the level of required agitation generally increases; i.e. more power is necessary to overcome the viscous forces. In this study, we have highlighted that to sufficiently mix a fluid (either Newtonian or non-Newtonian) within an OBC, a plane-averaged velocity ratio less than 3.5 is required. In the scale of the oscillatory Reynolds numbers experimented, this means that the OBC is capable of mixing viscous fluids at majority operating conditions.

6. Conclusions

We have presented flow patterns of Newtonian and non-Newtonian fluids in the OBC using both DPIV and CFD techniques. The effects of viscosity on mixing are sequentially examined through analysing flow patterns generated by both CFD simulation and DPIV measurements. A ratio of the plane-averaged axial over the radial velocity is defined to quantify such the viscosity effects. For the given geometry the velocity ratio approaches to 2 very quickly at increased oscillatory Reynolds numbers, regardless of Newtonian and non-Newtonian fluids. An empirical critical value of $R_v = 3.5$ is identified, below which the system mixes sufficiently. This would act as a guide for industrial applications where a viscous fluid is mixed in an aqueous solution in the OBC.

Acknowledgement

The authors wish to thank EPSRC for the funding in connection to this project.

References

[1] A.B. Metzner, R.E. Otto, Am. Inst. Chem. Eng. J. 3 (1) (1957) 3–10.

[2] A.B. Metzner, J.S. Taylor, Flow Patterns in agitated vessels, Am. Inst. Chem. Eng. J. 6 (1960) 109–114.

[3] G.S. Armstrong, S. Ruszkowski, Measurement and comparison of flows generated by different types of impeller in a stirred tank, in: Proceedings of Colloquium on Mechanical Agitation, Toulouse, France, 1987.

[4] V.V. Ranada, J.B. Joshi, Flow generated by pitched blade turbines I: measurements using laser Doppler anemometer, Chem. Eng. Commun. 81 (1989) 197–224.

[5] Z. Jaworski, A.W. Nienow, E. Koutsakos, K. Dyster, W. Bujalski, An LDA study of turbulent flow in a baffled vessel agitated by a pitched blade turbine, Trans. Inst. Chem. Eng. 69 (1991) 313–320.

[6] S.M. Kresta, P.E. Wood, The mean flow field produced by a 45° pitched blade turbine: changes in the circulation pattern due to off bottom clearance, Can. J. Chem. Eng. 71 (1993) 42–53.

[7] R.M. Hockey, J.M. Nouri, Turbulent flow in a baffled vessel stirred by a 60° pitched blade impeller, Chem. Eng. Sci. 51 (1996) 4405–4421.

[8] J.M. Nouri, R.M. Hockey, Power number correlation between Newtonian and non-Newtonian fluids in a mixing vessel, J. Chem. Eng. Jpn. 31 (1998) 848–852.

[9] T. Howes, On the Dispersion of Unsteady Flow in Baffles Tubes, PhD Thesis, The University of Cambridge, 1988.

[10] M.R. Mackley, X. Ni, Mixing and dispersion in a baffled tube for steady laminar and pulsatile flow, Chem. Eng. Sci. 46 (12) (1991) 3139–3151.

[11] X. Ni, P. Gough, On the discussion of the dimensionless groups governing oscillatory flow in a baffled tube, Chem. Eng. Sci. 52 (1997) 3209–3212.

[12] R.J. Adrian, Particle-imaging techniques for experimental fluid mechanics, Annu. Rev. Fluid Mech. 23 (1991) 261–304.

[13] R.J. Adrian, Bibliography of particle velocimetry using imaging methods: 1917–1995, University of Illinois, USA, 1996.

[14] M. Raffel, C. Willert, J. Kompenhans, Particle Image Velocimetry, A Practical Guide, Springer-Verlag, New York, 1998.

[15] X. Ni, H. Jian, A.W. Fitch, CFD modelling of flow patterns in an oscillatory baffled column, Chem. Eng. Sci. 57 (2002) 2849–2862.

[16] Fitch, A.W. Characterisation of Flow in an Oscillatory Baffled Column Using Digital Particle Image Velocimetry and Laser Induced Fluorescence, PhD Thesis, Heriot-Watt University, Edinburgh, 2003.

[17] X. Ni, H. Jian, A.W. Fitch, Evaluation of turbulent integral length scale in an oscillatory baffled column using large-eddy simulation and digital particle image velocimetry, Trans. Inst. Chem. Eng. 81 (A8) (2003) 842–853.

[18] H.L. Greene, C. Carpenter, L. Casto, Mixing characteristics of an axial impeller with Newtonian and non-Newtonian fluids, 4th European Conference on Mixing, Noordwijkerhout, Netherlands, April 27–29, 1982.

[19] J.M. Nouri, R.M. Hockey, Flow characteristics of Newtonian and non-Newtonian fluids in a vessel stirred by a 60° pitched blade impeller, J. Chem. Eng. Jpn. 40 (2001) 454–459.